Research Article Vol. 3, No. 7 / 15 July 2020 / OSA Continuum 1739

Optical coherence tomography with balanced signal strength across the depth for pearl inspection

HUADE MAO,[1] PINGPING FENG,[1] YU-XUAN REN,[1] JIQIANG KANG,[1] KEVIN K. TSIA,[1] WA-TAT YAN,[2] AND KENNETH K. Y. WONG[1,*]

[1]*Department of Electrical and Electronic Engineering, The University of Hong Kong, Pokfulam Road, Hong Kong*
[2]*The Swire Institute of Marine Science and School of Biological Sciences, The University of Hong Kong, Pokfulam Road, Hong Kong*
[*]*kywong@eee.hku.hk*

Abstract: Optical coherence tomography (OCT) relies on the reflection of light from structures in different layers to interferometrically reconstruct the volumetric image of the sample. However, light returned from multiple layers suffers from imbalanced attenuation owing to the optical path difference and inhomogeneous tissue absorption. We report an optimization algorithm to improve signal strength in deep tissue for swept-source (SS)-OCT imaging. This algorithm utilizes the attenuation coefficient of consecutive layers within the sample and combines them to compensate for the signal intensity loss from deep tissue. We stacked 170-μm thick cover slides as a standard sample for benchmark testing. The optimized OCT image provides a 30% increase in signal intensity in the deep structure compared with the conventional images. We applied this method for pearl inspection, whose layered structure demonstrates a great application for our optimized OCT imaging. In contrast to X-ray micro-CT scan and scanning electron microscope (SEM) imaging modalities, the optimized OCT imaging provides great potential for pearl quality inspection. The proposed improvement algorithm for SS-OCT could also be applied to diverse biomedical imaging scenarios, including label-free tissue imaging.

1. Introduction

Optical coherence tomography (OCT) has been widely applied in deep tissue imaging [1], disease diagnosis [2], etc., ever since its invention in the 1990s [3]. To date, it is continually being enhanced in many aspects, including resolution [4], imaging depth [5,6], and imaging speed [7]. Although it is noninvasive [8] and label-free [9], the OCT, in general, suffers from image distortion and signal imbalance [10,11], due to, for example, the multiple light scattering from the inhomogeneity of the sample [12]. Usually, such distortion is introduced by the refractive error [13], optical scattering [14], and depth axial attenuation [15]. For refractive error, ray-tracing tools [16] are well-developed and could achieve an accuracy of less than 5×10^{-3} reconstruction error [17]. Meanwhile, a depth-dependent function was proposed to extract the optical scattering coefficient [14], which features to give the depth-dependent heterodyne current [18]. In particular, the depth axial attenuation, among all the distortion factors, has attracted substantial attention, since it is frequently encountered in OCT technique and closely associated with refraction and scattering. Based on the single scattering model, an algorithm is proposed to calculate the attenuation coefficient [15]. By a multi-angle scan, the image distortion from axial attenuation could also be eliminated [19]. As photon propagates randomly in a homogenous medium, a Monto Carlo model can retrieve the signal attenuation and provide calibrated data for compensation of

#394157 https://doi.org/10.1364/OSAC.394157
Journal © 2020 Received 1 Apr 2020; revised 9 Jun 2020; accepted 11 Jun 2020; published 18 Jun 2020

OSA CONTINUUM

the distortion in OCT images [20]. The attenuation coefficients from existing OCT images could aid to model the axial attenuation to discriminate different tissues [21].

However, most optimization schemes focus on general sample detection. As the performance of one scheme may vary on different sample categories, it is more practical to give a specific solution of a certain sample category of interest. Some works have been demonstrated along this direction with the phantom samples ranging from micro-vasculature [22], slow-rate strains [23], to vascular quantification [24], etc. When it comes to pearls, which is of great artistic value and in need of non-destructive inspection, OCT-based noninvasive detection schemes were also explored, including nacre thickness measurement and nuclei identification [25], defect analysis [26], and treatment investigation [27]. Nevertheless, these schemes adopt the general OCT technique. They could perform better if the OCT is specifically optimized for layered samples like pearls [28].

Here in our work, we report an optimization algorithm called layer-based compensation algorithm (LaB-CA), integrated to the SS-OCT modality, to compensate for the imbalanced attenuation of signal strength from depth. Firstly, a phantom sample, consisting of a stack of cover slides, is investigated to imitate pearls' layered structure. Then, the optimized imaging results of pearls are demonstrated in comparison with X-ray micro-CT images and scanning electron microscope (SEM) images. Our LaB-CA algorithm readily compensates for the layer-dependent attenuation. The results show that LaB-CA is a promising solution for layer-structured samples and specifically, a potential aid for quality inspection and type differentiation in pearls jewelry industry.

2. Theory and experimental setup

The working principle of our LaB-CA optimized OCT can be simply explained in Fig. 1(a), in which the scattering center is supposed to be in each of the multiple layers. As the beam penetrates inside the multiple layers, the light intensity experiences variable attenuation according to the number of layers and the density of the scattering center.

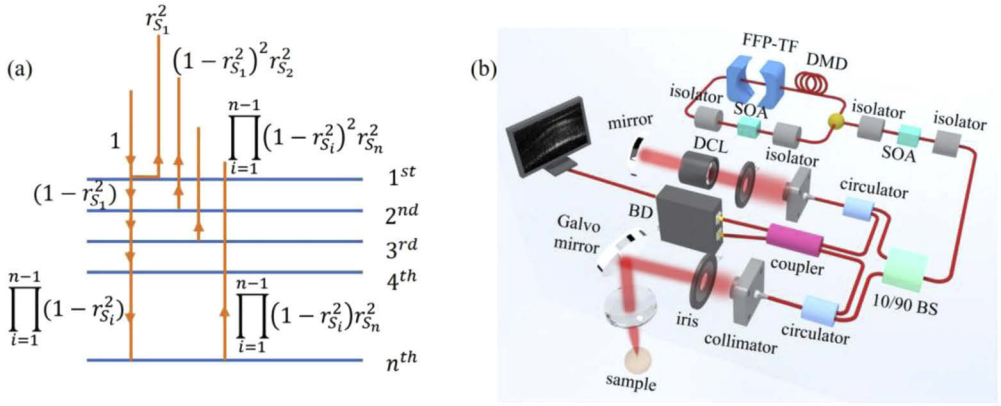

Fig. 1. (a) Theoretical model: measured reflected signal intensity at different layers in terms of their reflection coefficients. We assume the incident signal intensity is unity. (b) Experimental SS-OCT setup. FFP-TF: fiber Fabry-Perot tunable filter; DMD: dispersion-managed delay; SOA: semiconductor optical amplifier; DCL: dispersion compensation lens; 10/90 BS: 10/90 beam splitter; coupler: 50/50 coupler; BD: balanced detector.

To understand our LaB-CA algorithm, we first briefly review the basic principle of OCT [29]. The incident beam has an electric field of $E_i = S(k) \cdot \exp(i(kz - \omega t))$, where S(k) denotes amplitude depending on the wavenumber k. After the light goes through a beam splitter with

OSA CONTINUUM

splitting ratio a/b, the electric field becomes

$$E_R = \sqrt{\frac{a}{a+b}} E_i r_R e^{i\cdot 2kz_R}, \tag{1}$$

$$E_S = \sqrt{\frac{b}{a+b}} E_i \sum\nolimits_{n=1}^{N} r_{S_n} e^{i\cdot 2kz_{S_n}}, \tag{2}$$

where E_R and E_S represent the electric field in the respective reference and sample arm, z_R and z_{Sn} denote the distance from the beam splitter (as they set z=0 at the beam splitter), r_R and r_{Sn} are the electric field reflection coefficient in the reference arm and sample arm dependent on the sample's depth.

Here is how our LaB-CA differs from literature. As the beam penetrates the sample, the reflected light from a certain depth, which is considered a layer through the whole manuscript, has undergone the attenuation of the previous layers. It means that the electric field reflection coefficient upon detection is the attenuated one, and our LaB-CA aims at compensating the reflectivity, thus getting a more balanced signal.

We assume the electric field reflection coefficient of each layer within the sample is R_{S_i}, consequent power reflection being $R_{S_i}^2$, where i denotes the order of layers. In Fig. 1(b), if the intensity of the incident beam is unity, it will be reduced to $\prod_{i=1}^{n-1}(1 - R_{S_i}^2)$ when it reaches n^{th} layer after attenuation by previous $(n-1)$ layers.

Once reflected, the beam goes through the $(n$ - 1) layers again and the intensity is reduced by a factor of $\prod_{i=1}^{n-1}(1 - R_{S_i}^2)R_{S_n}^2$ at the detector. The detected intensity for the n^{th} layer is

$$r_{S_n}^2 = \prod\nolimits_{i=1}^{n-1} (1 - R_{S_i}^2)^2 R_{S_n}^2. \tag{3}$$

Here R_{S_n} is the actual electric field reflection coefficient whereas r_{S_n} is the nominal one used in the literature [3,29]. Obviously in Eq. (3), r_{S_n} is less than R_{S_n}, OCT usually suffers from attenuated signal intensity in depth [30].

After the reference light and sample light converge at the balanced detector, the current reads $i(z) = \frac{\rho b}{2(a+b)} \gamma(z) \sum_{n=1}^{N} r_{S_n}^2$, upon which the OCT image is obtained [29], where $\gamma(z)$ is the Fourier transform of S(k). Since the current $i(z)$ is proportional to the power reflectivity $r_{S_n}^2$, we could compensate for the signal intensity in the same manner on power reflectivity.

For the 1st layer, the surface of the sample, the actual electric field reflectivity R_{S_1} is equal to its nominal reflectivity r_{S_1}. From the 2nd layer and onwards, the nominal power reflectivity $r_{S_2}^2$ could be replaced with their actual power reflectivity, which is

$$R_{S_n}^2 = \frac{r_{S_n}^2}{\prod_{i=1}^{n-1}(1 - R_{S_i}^2)}. \tag{4}$$

After iteratively retrieving the previous layers' power reflectivity, the whole sample's power reflectivity of different layers' depth could be renewed. For the obtained OCT image, we conduct the LaB-CA methods for each A-line. The image is transformed into a normalized gray-scale image, with one pixel standing for 14 μm depth which is considered as one layer.

The highest gray-scale value, which is usually located at the surface of the sample, is calibrated to a known power reflection coefficient, in a linear way similar to this work [31], which combined a tissue and a reflecting planar surface together to compare their optical path. Our calibration is a self-referenced method. The parameter k is retrieved as the ratio of the highest gray value and the reflection coefficient. Then the whole image, representing in gray value, is divided by the parameter k to get the calibrated reflection coefficient. Here for example, a phantom sample, consisting of 10 cover slides in Fig. 2, is adopted to calibrate the surface power reflection

OSA CONTINUUM

coefficient at 0.04. Afterwards, the whole image is divided by the same coefficient to get the calibrated reflection coefficient. We set the detected power reflectivity, which is gray-scale value in the image, as g_{S_n}. Since the surface power reflectivity $g_{S_1} = G_{S_n}$ is 0.04, the second and onward layer power reflectivity could be compensated as

$$G_{S_n} = \frac{g_{S_n}}{\prod_{i=1}^{n-1}(1 - G_{S_i})}, \tag{5}$$

where G_{S_n} is the new power reflection coefficient through our LaB-CA algorithm. In this way, the power reflection coefficient, which is proportional to signal intensity, could be balanced at different detected depth.

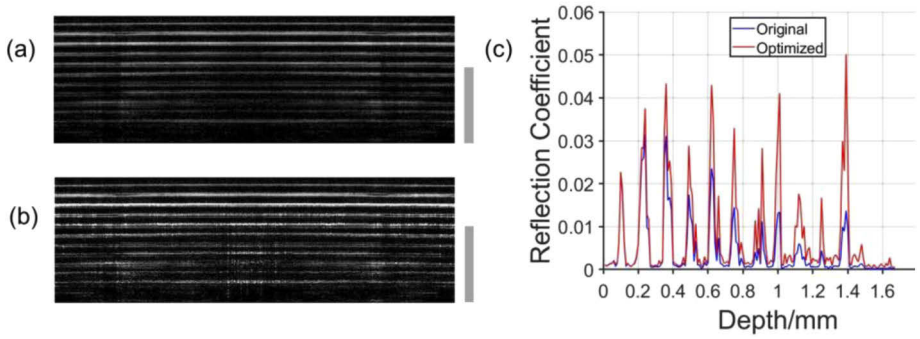

Fig. 2. (a) Original scanning result of standard cover slides with a thickness of 170 µm. (b) Optimized results after our LaB-CA method. (c) Normalized signal intensity comparison extracted from the imaging results. Scale bar: 1 mm.

Figure 1(b) shows our experimental SS-OCT setup based on Michelson-interferometer. The theory of SS-OCT was well discussed previously [29]. We built a Fourier-domain mode-locking (FDML) laser system [32,33]. The fiber Fabry-Perot tunable filter (FFP-TF) (Wolftek, Inc.) generates an optical spectrum of ~80 nm bandwidth centered at 1,500 nm. The semiconductor optical amplifier (SOA) (Inphenix, Inc.) inside and outside the cavity serves as a gain medium and power booster, respectively. The direct output average power of the laser was 3 mW and was split by a 90/10 beam splitter. The 10% power was used in the reference arm, while the pulses with the remaining 90% power were collimated into the sample arm. In the reference arm, the beam passes through dispersion compensator (LSM03DC, Thorlabs, Inc.) and retro-reflected by a flat mirror. In the sample arm, the beam was steered by a pair of galvo mirrors (GSV102, Thorlabs, Inc.) and focused by a scanning lens (LSM03, Thorlabs, Inc.) onto the sample. Owing to the axial resolving ability by the optical spectrum, the volumetric imaging only requires the scanning of the beam in two dimensions. The reflected beam from both the sample and the reference arms were collected by the same collimators and went through the 50/50 fiber coupler. The interferometric signal was digitized by the balanced detector (BD: PDB110C-AC, Thorlabs, Inc.) for off-line image processing. The resolution of the OCT setup is 14 µm and sensitivity is 85 dB over 0-3 mm depth without obvious change, which are elaborated in our previous work [32].

To test our algorithm and retrieve the calibrated reflection coefficient, we run a benchmark experiment to collect the SS-OCT signal retroreflected from the standard sample. Here we prepared a stack of 10 cover slides with a thickness of 170 µm each. The original SS-OCT image [Fig. 2(a)] suggests a significant intensity decrease with respect to the depth. In the presence of our LaB-CA optimization, the SS-OCT image becomes more uniform across the whole imaging depth [Fig. 2(b)]. From 3^{rd} layer and onwards (from top to bottom) in Fig. 2(b), the signal

OSA CONTINUUM

strength of each layer has increased by more than 30%. Cover slides, composed of glass, have a reflection coefficient of 0.04. As the focus of the reference beam is not exactly at the surface, the highest intensity in Fig. 2(c) is the third layer, which was taken as the calibrated power reflection coefficient. To emphasize, no other noise reduction procedure has been applied in our algorithm to suppress the speckle effect [34], as LaB-CA is a self-referenced compensation scheme. Such algorithm could potentially be combined with other OCT image correction methods. Figure 2(c) demonstrates the linear intensity profile, which is converted to the reflection coefficient along the axial direction before (blue) and after (red) compensation. The intensity becomes more uniform after LaB-CA algorithm. Most spikes are close to the reflection coefficient at 0.04, despite the spikes located at about 1.1 mm and 1.3 mm due to their originally weak signal. The average reflection coefficient is 0.036 (0.019) after (before) compensation, which means the LaB-CA provides a 42.5% higher accuracy on the signal intensity. Since the LaB-CA is to compensate for the weaker signal in deeper tissue rather than fill in the undetected depth beyond, technically the detection depth remains unchanged.

3. Results and discussion

Here we applied the LaB-CA for noninvasive inspection of the pearls (Fig. 3). The LaB-CA optimized OCT does have an improvement over SS-OCT. The pearls under inspection (Fig. 3) are (a-d) freshwater pearl, (e-h) Akoya pearl (seawater pearl), (i-l) black pearl (seawater pearl). For each pearl, we collected its SS-OCT, LaB-CA optimized OCT, micro-CT (computed tomography), SEM (Hitachi S-3400N), and signal extraction data, which were listed in the same row as shown in Fig. 3. The micro-CT machine (SKYSCAN 1172 X-ray Microtomograph, Bruker Inc.) is set at 10 μm scanning resolution.

For the freshwater pearl in Figs. 3(a)–3(d), the real image of the sample is shown on the bottom left corner of Fig. 3(a). The LaB-CA optimized OCT improves over SS-OCT, in which the signal strength at depth from 0.6 mm to 1.1 mm is stronger than that in original SS-OCT, enabling the visualization of another layer structure beyond the lower nacre. The same pearl sample has also been inspected by micro-CT at the cost of a longer time (~ hours for a resolution of 10 μm). The micro-CT image close to the edge is shown in Fig. 3(b). Although the micro-CT was able to inspect the whole structure of the large pearl sample (~5 mm in diameter), the resolution is insufficient to observe the details. We also applied the SEM to inspect the nacre structure with high image precision. However, the sectional image requires to break the pearls sample to visualize the section. The typical thickness of one nacre layer for the freshwater pearl is roughly 200 μm. We plot the linear intensity profiles from the SS-OCT image with (and without) optimization, and a multi-Gaussian fit to the intensity demonstrating that the FWHM (i.e., full width at half maximum) of about 0.2 mm (0.25 mm). The thickness evaluated from the original SS-OCT image over-estimates the nacre thickness. The FWHM retrieved from the optimized image corresponds to the thickness of a single nacre layer, and is consistent with the layer thickness evaluated under SEM. In Fig. 3(d), the optimized signal has roughly 8 narrow sharp peaks from 0.45 mm to 0.7 mm in the second Gaussian-like peak. It may give more information on the nacre structure about which the original signal can hardly tell.

The consistency of the layer thickness measurement between the optimized OCT and the SEM has been further corroborated with an Akoya pearl grown in seawater. Figure 3(e) shows the OCT images of the Akoya pearl (photo at the bottom left corner shows the real sample). Similarly, the LaB-CA optimized OCT image shows a clearer and more uniform nacre than the original SS-OCT image. The micro-CT image with uniform signal strength is insufficient to identify the minute structure owing to the lack of resolution (~ 10 μm). The thickness of the nacre layer is evaluated to be about 100 μm under SEM [Fig. 3(g)]. We further extracted the linear signal [Fig. 3(h)], which suggests distinct layers located at 0.38 mm, 0.48 mm, and 0.6 mm. Therefore, the thickness in FWHM matches well with SEM measurement. As for the original signal, the

OSA CONTINUUM

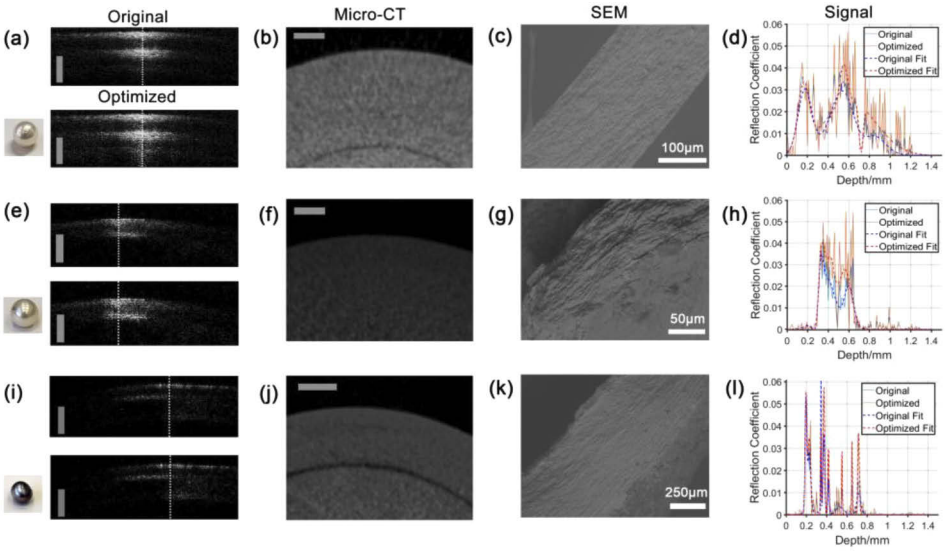

Fig. 3. The original SS-OCT, LaB-CA optimized OCT, X-ray micro CT, SEM images, and signal extraction of different pearls: (a-d) freshwater pearl, (e-h) Akoya pearl (seawater pearl), (i-l) black pearl (seawater pearl). (a, e, i) The OCT images without (top) and with (bottom) optimization. The bottom left corner shows the respective real image of the pearl sample. (b, f, j) The micro-CT images show the morphology of each pearl close to the surface. (c, g, k) SEM images demonstrate the detailed layered structure close to the surface. (d, h, l) The linear OCT signal profile (including original and optimized signal, and Gaussian fit) for each pearl. Scale bar in the first and second column denotes 500 μm. The white scale bar on SEM images represents (c) 100 μm, (g) 50 μm, and (k) 250 μm.

dips at the mentioned places may be too tiny to be identified as a layer boundary. In each layer, there are nearly 3 peaks at the optimized signal, which is quite limited compared to SEM but gives more information than that of the original one.

We take the black pearl as the second seawater sample [Fig. 3(i)], and found that the LaB-CA reinforces slightly on subtle structures displayed in the SS-OCT image. Although we can see the growth ring in the micro-CT image, finer details are impossible to identify. The nacre layer structure has been imaged under the SEM [Fig. 3(k)], which suggests a thickness of the black pearl of around 600 μm. In contrast, the effective signal from the optimized OCT image starts from 0.19 mm to about 0.70 mm [Fig. 3(l)]. The consistency of the thickness measurement with LaB-CA optimized OCT and the SEM suggests the feasibility of using the OCT to estimate the layer thickness without breaking the pearl sample itself. It also suggests that the nacre of this black pearl did not fall apart into layers when we cut it. From the Gaussian fit line [Fig. 3(l)], it implies that the black pearl may have 8 layers. If it comes to the original signal, the layer peak located at 0.55 mm and 0.65 mm may be neglected and the original signal ranging from 0.45 mm to 0.60 mm can only give a very limited amount of information due to the weak signal.

Our LaB-CA improves the intensity of original SS-OCT by at least 15% at a deep nacre layer and gives more accurate results on layer thickness and growth rings, which is further validated by micro-CT and SEM. Based on our LaB-CA optimized results of nacre thickness, growth rings, and reflection coefficient, the jewelry industry may have a better judgment over pearls' type.

Secondly, as the quality inspection is of crucial importance in the modern jewelry business, we elect two Akoya pearls (one 'bad' pearl and one 'good' pearl judged by a merchant) for

OSA CONTINUUM

demonstration. Figure 4 shows the imaging results with (a-d) for the bad Akoya pearl and (e-h) for the good Akoya pearl. These two pearls are different from what has been shown in Fig. 3.

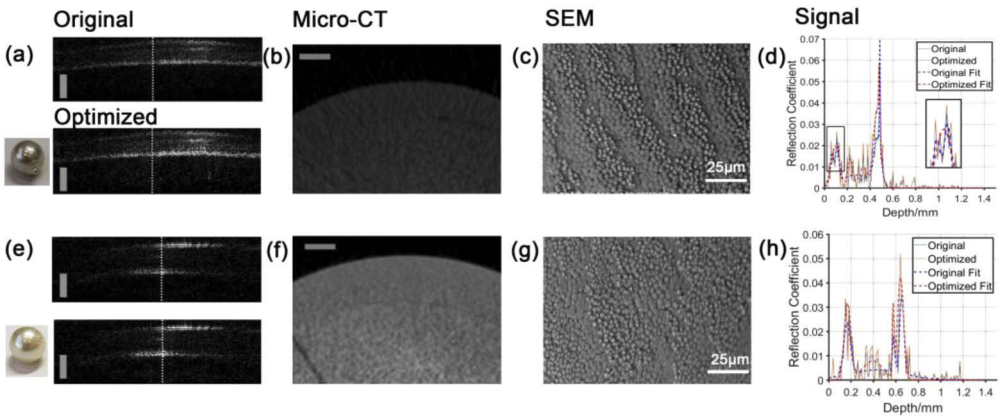

Fig. 4. Scanning results of two specific pearls, (a-d) bad Akoya pearl, and (e-h) good Akoya pearl. In each row, the data type is the same, viz, SS-OCT data in the first column with the top being original and the bottom being the LaB-CA optimized one, micro-CT scan data in the second column, surface SEM data in the third column, and signal extraction (including signals and their respective Gaussian fit) in the fourth column. The grayscale bar in the first and second column denotes 400 μm, while the white gray bar in (c) and (g) denotes 25 μm.

The micro-CT was able to provide an overall view of the whole nacre, which is consistent with the images shown in Figs. 4(a) and 4(e), but fails to give more detailed information. For the bad Akoya pearl in Fig. 4(d), the signal peaks at 0.22 mm and 0.35 mm of LaB-CA optimized fit is overlooked by the original SS-OCT signal, which is due to the relatively low signal strength in this region. At 0.1-mm depth, the LaB-CA optimized fit has only one peak while the original SS-OCT has two peaks. From SEM images in Fig. 3(c) of the surface, the granule of the pearl is sparsely and evenly distributed, which means the layers should have an even distribution along the depth. In that sense, our LaB-CA optimized fit is more reasonable with layer peaks roughly equally spaced along 0 to 0.6 mm than the original SS-OCT.

For the good Akoya pearl in Fig. 4(h), the 3 spikes located from 0.3 mm to 0.45 mm have a different impact on the Gaussian fitting. For LaB-CA, a peak is shown, which may suggest a layer, while no peak is plotted on original SS-OCT due to the below-threshold signal strength (0.01 is set as the threshold). Other 3 peaks at 0.15 mm, 0.57 mm, and 0.65 mm, the LaB-CA signal all have at least 20% higher strength than original OCT. From the SEM image in Fig. 4(g), the granule distribution is denser, leading to a lower reflection for the layers between upper and lower boundaries. Therefore, it can be well explained that the peak at 0.4 mm has an apparent gap compared to the other 3 peaks.

Above all, the LaB-CA optimized OCT may have potential use in quality grading. For the original OCT signal of these two pearls, both show a flat trend from 0.2 mm to 0.4 mm, which is not enough to tell the difference. For LaB-CA optimized OCT, the equally distributed peaks similar to Fig. 4(d) may suggest a sparse distribution of the nacre, which is a sign of bad quality. And the 'U'-shape signal, which means the middle signal is much lower than the boundary signals, may suggest the granule is densely distributed and possibly of better quality. Surely, more sample pearls could be selected to set a quality ranking library, to further develop this algorithm.

Thirdly, to validate the improvement of our LaB-CA algorithm, we performed the perception-based image quality evaluator (PIQE) to compare the image quality improvement owing to our optimization algorithm. The PIQE score is used to determine image quality without reference

OSA CONTINUUM

[35] by dividing an image into nonoverlapping blocks, extracting the local features to classify whether it is distorted by a preset threshold, and finally providing a PIQE score as a mean of all values from these blocks. In PIQE, a lower score represents a higher quality. The PIQE score for the pearls of all the sizes we imaged with SS-OCT and processed using the LaB-CA algorithm are shown in Fig. 5. In summary, our LaB-CA improves the image quality, or reduces the PIQE score, at about 5 in absolute value, which supports the conclusion that the signal imbalance compensation greatly improves the image quality.

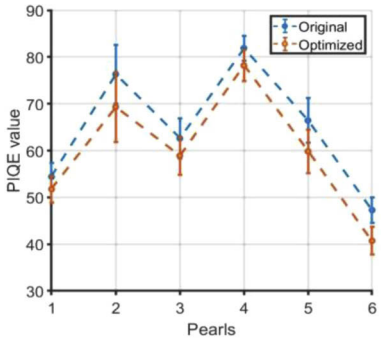

Fig. 5. PIQE score for the OCT images of the pearl samples, and a lower score represents a higher quality. The blue line denotes original OCT images while the orange line represents the LaB-CA optimized OCT images. In the x-axis, each number stands for different pearls. 1: Freshwater pearl; 2: black pearl; 3-6: different Akoya pearls. (3: the Akoya pearl in Fig. 3(e); 4: the bad Akoya pearl in Fig. 4(a); 5: the good Akoya pearl in Fig. 4(b).)

4. Conclusion

In conclusion, we reported a LaB-CA algorithm incorporated into SS-OCT to optimize the signal intensity from deeper tissue and displayed its use in pearl imaging to differentiate their types and evaluate their quality. The LaB-CA algorithm considers each layer's scattering and attenuation, then compensates the loss to the deeper layer. It is suitable for those layer-structured samples, e.g., pearls in particular. The benchmark test with standard cover slide stack using LaB-CA suggested an improvement of 30% in signal intensity from the 3rd layer and onwards compared to original SS-OCT. Then we applied it to pearl imaging and demonstrated good correspondence with X-ray micro-CT and SEM image. We showed that our LaB-CA improves the image quality with PIQE score reduced by nearly 5 in absolute value or 8% in ratio. However, since no noise reduction is adopted during the process, LaB-CA will compensate the noise as well. Though it performs well in enhancing signal intensity, it is suggested to have the noised reduced before applying LaB-CA. Another limit is LaB-CA is suitable for layer-structured samples, which are pearls in this manuscript. When it comes to samples with complex optical properties beyond the single reflection model adopted here, other model is needed or incorporated into LaB-CA to better suit that sample category's imaging.

In contrast to the X-ray phase imaging and neutron imaging [36], the SS-OCT equipped with our LaB-CA algorithm is readily suitable for the non-invasive and label-free inspection of the pearl. LaB-CA optimization has great potential to reveal the relationship between signal trend versus category and quality. In the future, more pearls could be elected to generate different classifications of category and quality [37] for further experiments, to give a general rule of signal trend and pearls' property, e.g., type, origin, and quality. And existing SS-OCT techniques for pearls investigation [26] could benefit from the LaB-CA optimization for more accurate and quantified results.

OSA CONTINUUM

Appendix A.

Lab-CA optimized OCT scanning results for different samples

To validate our algorithm, we apply the LaB-CA optimized OCT to other samples, apart from the pearl samples mainly discussed in the script.

First, cellulose, which is paper in this experiment, is investigated in Fig. 6. The thickness of one paper is 0.12 mm, as 70 papers are measured of an 8.50 mm thickness. Figures 6(a) and 6(b) present the results of 10 papers, while Figs. 6(c) and 6(d) is about 12 papers. Because of the high absorption of cellulose, the major component of papers, the retrieved signal has decreased after 0.4 mm penetration, which is about 4-paper thickness. For 10-paper results in Fig. 6(b), our LaB-CA optimized OCT data's Gaussian fit has 3 peaks, representing that 3 papers are located in the 0.2 mm to 0.5 mm range, while the original SS-OCT data only shows one peak at 0.2 mm, failing to retrieve the correct information. As the signal's intensity drops dramatically after 0.6 mm, it's acceptable the fourth paper located at 0.6 mm cannot be drawn. For the 12-paper results in Fig. 6(d), our LaB-CA algorithm could identify 2 peaks between 0.2 mm and 0.4 mm, which is correspondent with the paper's thickness measured before. However, the original SS-OCT, still, fails to give useful information and only shows 1 peak at 0.2 mm.

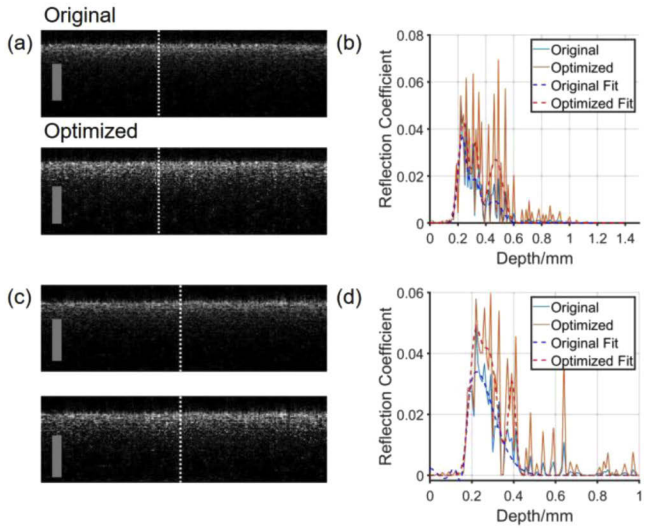

Fig. 6. OCT scanning results on papers. (a, b) Results for 10 papers as a sample. (c, d) Results for 12 papers as a sample. (a, c) The top image is the original SS-OCT result, and the lower image is our LaB-CA optimized OCT result. (b, d) Extracted signal, along with their Gaussian fit, from the white line in (a) and (c). The grayscale bar is 0.5 mm.

Second, biological fiber, which is lean pork in Figs. 7(a) and 7(b) and fatty pork in Figs. 7(c) and 7(d) here, is examined under LaB-CA optimization OCT. For the lean pork, the second peak improvement of LaB-CA optimized image at 0.35 mm is quite obvious in Fig. 7(b). From 0.4 mm and onwards, the LaB-CA optimized fit may indicate another layer, which is the muscle fiber for this sample, while the original SS-OCT fit just decreases to zero. Besides, for the fatty pork in Fig. 7(d), the LaB-CA optimized OCT indicates a layer at 0.72 mm while the original SS-OCT fails. For the peak located at 0.3 mm and 0.9 mm, the optimized fit has a nearly 5% and 21% intensity increase respectively compared to original SS-OCT.

OSA CONTINUUM

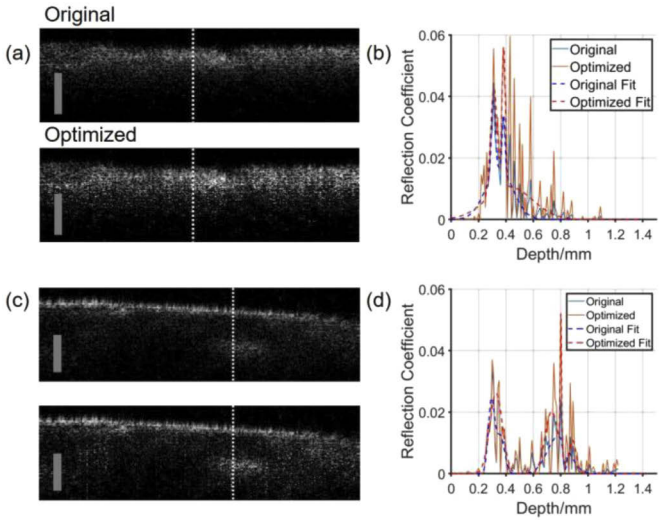

Fig. 7. OCT scanning results on lean and fatty pork. (a, b) Results for the lean pork. (c, d) Results for the fatty pork. (a, c) The top image is the original SS-OCT result, and the lower image is our LaB-CA optimized OCT result. (b, d) Extracted signal, along with their Gaussian fit, from the white line in (a) and (c). The grayscale bar is 0.5 mm.

Appendix B.

Elaboration on the scanning results of freshwater pearl in Fig. 3(d)

Four A-line is chosen as in Fig. 8. The position of the selected A-line is shown in Fig. 8(a). The corresponding results are demonstrated in the order of Figs. 8(b), 8(c), 8(d), and 8(e) as the position moves from left to right.

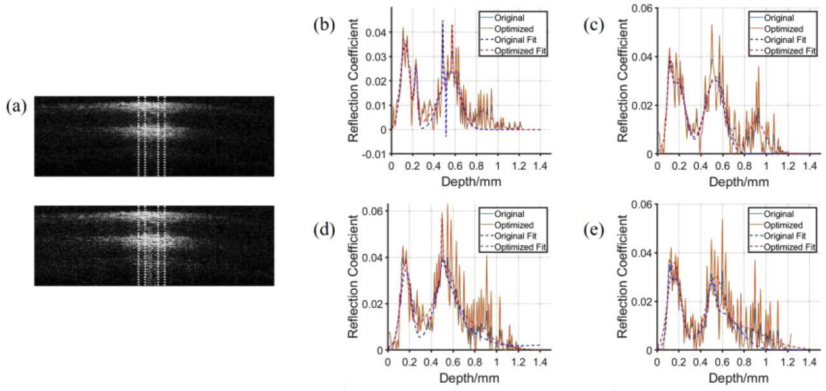

Fig. 8. Different A-line scanning results on the freshwater pearl. (a) Position of A-lines. (b, c, d, e) Processed results as the position moves from left to right.

From Fig. 8, in the depth from 0.45 mm to 0.70 mm, the numbers of sharp peaks are 9, 7, 9, 9 respectively in Figs. 8(b), 8(c), 8(d), and 8(e). Combined with Fig. 3(d), LaB-CA could reveal the nearly 8 sharp peaks' information after self-compensation. For the SEM image in Fig. 3(c), the nacre has finer layers, which are beyond LaB-CA and original SS-OCT's capacity.

OSA CONTINUUM

Funding

Research Grants Council, University Grants Committee (CityU T42-103/16-N, E-HKU701/17, HKU 17200219, HKU 17209018, HKU C7047-16G); National Natural Science Foundation of China (N_HKU712/16).

Acknowledgments

We appreciate the help from Electron Microscopy Unit at Queen Mary Hospital of HKU for the electron microscopy imaging, and the Faculty of Dentistry at HKU for X-ray microtomography of the pearls.

Disclosures

The authors declare no conflicts of interest.

References

1. Y. Zhao, W. J. Eldridge, J. R. Maher, S. Kim, M. Crose, M. Ibrahim, H. Levinson, and A. Wax, "Dual-axis optical coherence tomography for deep tissue imaging," Opt. Lett. **42**(12), 2302–2305 (2017).
2. M. T. Leite, L. M. Zangwill, R. N. Weinreb, H. L. Rao, L. M. Alencar, P. A. Sample, and F. A. Medeiros, "Effect of Disease Severity on the Performance of Cirrus Spectral-Domain OCT for Glaucoma Diagnosis," Invest. Ophthalmol. Visual Sci. **51**(8), 4104–4109 (2010).
3. D. Huang, E. A. Swanson, C. P. Lin, J. S. Schuman, W. G. Stinson, W. Chang, M. R. Hee, T. Flotte, K. Gregory, C. A. Puliafito, and J. G. Fujimoto, "Optical coherence tomography," Science **254**(5035), 1178–1181 (1991).
4. G. J. Tearney, M. E. Brezinski, B. E. Bouma, S. A. Boppart, C. Pitris, J. F. Southern, and J. G. Fujimoto, "In Vivo Endoscopic Optical Biopsy with Optical Coherence Tomography," Science **276**(5321), 2037–2039 (1997).
5. A. Badon, D. Li, G. Lerosey, A. C. Boccara, M. Fink, and A. Aubry, "Smart optical coherence tomography for ultra-deep imaging through highly scattering media," Sci. Adv. **2**(11), e1600370 (2016).
6. N. M. Israelsen, C. R. Petersen, A. Barh, D. Jain, M. Jensen, G. Hannesschläger, P. Tidemand-Lichtenberg, C. Pedersen, A. Podoleanu, and O. Bang, "Real-time high-resolution mid-infrared optical coherence tomography," Light: Sci. Appl. **8**(1), 11 (2019).
7. M. Siddiqui, A. S. Nam, S. Tozburun, N. Lippok, C. Blatter, and B. J. Vakoc, "High-speed optical coherence tomography by circular interferometric ranging," Nat. Photonics **12**(2), 111–116 (2018).
8. Y. Shimada, H. Nakagawa, A. Sadr, I. Wada, M. Nakajima, T. Nikaido, M. Otsuki, J. Tagami, and Y. Sumi, "Noninvasive cross-sectional imaging of proximal caries using swept-source optical coherence tomography (SS-OCT) in vivo," J. Biophotonics **7**(7), 506–513 (2014).
9. U. Baran, W. Qin, X. Qi, G. Kalkan, and R. K. Wang, "OCT-based label-free in vivo lymphangiography within human skin and areola," Sci. Rep. **6**(1), 21122 (2016).
10. N. Uribe-Patarroyo and B. E. Bouma, "Rotational distortion correction in endoscopic optical coherence tomography based on speckle decorrelation," Opt. Lett. **40**(23), 5518–5521 (2015).
11. S. Ortiz, D. Siedlecki, I. Grulkowski, L. Remon, D. Pascual, M. Wojtkowski, and S. Marcos, "Optical distortion correction in Optical Coherence Tomography for quantitative ocular anterior segment by three-dimensional imaging," Opt. Express **18**(3), 2782–2796 (2010).
12. S. Yoon, M. Kim, M. Jang, Y. Choi, W. Choi, S. Kang, and W. Choi, "Deep optical imaging within complex scattering media," Nat. Rev. Phys. **2**(3), 141–158 (2020).
13. A. Golabchi, J. Faust, F. N. Golabchi, D. H. Brooks, A. Gouldstone, and C. A. DiMarzio, "Refractive errors and corrections for OCT images in an inflated lung phantom," Biomed. Opt. Express **3**(5), 1101–1109 (2012).
14. D. Levitz, L. Thrane, M. H. Frosz, P. E. Andersen, C. B. Andersen, J. Valanciunaite, J. Swartling, S. Andersson-Engels, and P. R. Hansen, "Determination of optical scattering properties of highly-scattering media in optical coherence tomography images," Opt. Express **12**(2), 249–259 (2004).
15. K. A. Vermeer, J. Mo, J. J. A. Weda, H. G. Lemij, and J. F. de Boer, "Depth-resolved model-based reconstruction of attenuation coefficients in optical coherence tomography," Biomed. Opt. Express **5**(1), 322–337 (2014).
16. K. Minami, Y. Kataoka, J. Matsunaga, S. Ohtani, M. Honbou, and K. Miyata, "Ray-tracing intraocular lens power calculation using anterior segment optical coherence tomography measurements," J. Cataract Refractive Surg. **38**(10), 1758–1763 (2012).
17. A. de Castro, S. Barbero, S. Ortiz, and S. Marcos, "Accuracy of the reconstruction of the crystalline lens gradient index with optimization methods from Ray Tracing and Optical Coherence Tomography data," Opt. Express **19**(20), 19265–19279 (2011).
18. L. Thrane, H. T. Yura, and P. E. Andersen, "Analysis of optical coherence tomography systems based on the extended Huygens–Fresnel principle," J. Opt. Soc. Am. A **17**(3), 484–490 (2000).

OSA CONTINUUM

19. K. C. Zhou, R. Qian, S. Degan, S. Farsiu, and J. A. Izatt, "Optical coherence refraction tomography," Nat. Photonics **13**(11), 794–802 (2019).
20. D. J. Smithies, T. Lindmo, Z. Chen, J. S. Nelson, and T. E. Milner, "Signal attenuation and localization in optical coherence tomography studied by Monte Carlo simulation," Phys. Med. Biol. **43**(10), 3025–3044 (1998).
21. D. J. Faber, F. J. van der Meer, M. C. G. Aalders, and T. G. van. Leeuwen, "Quantitative measurement of attenuation coefficients of weakly scattering media using optical coherence tomography," Opt. Express **12**(19), 4353–4365 (2004).
22. A. Mariampillai, M. K. K. Leung, M. Jarvi, B. A. Standish, K. Lee, B. C. Wilson, A. Vitkin, and V. X. D. Yang, "Optimized speckle variance OCT imaging of microvasculature," Opt. Lett. **35**(8), 1257–1259 (2010).
23. V. Y. Zaitsev, L. A. Matveev, A. L. Matveyev, A. A. Sovetsky, D. V. Shabanov, S. Y. Ksenofontov, G. V. Gelikonov, O. I. Baum, A. I. Omelchenko, A. V. Yuzhakov, and E. N. Sobol, "Optimization of phase-resolved optical coherence elastography for highly-sensitive monitoring of slow-rate strains," Laser Phys. Lett. **16**(6), 065601 (2019).
24. M. Casper, H. Schulz-Hildebrandt, M. Evers, R. Birngruber, D. Manstein, and G. Hüttmann, "Optimization-based vessel segmentation pipeline for robust quantification of capillary networks in skin with optical coherence tomography angiography," J. Biomed. Opt. **24**(04), 1 (2019).
25. M. J. Ju, S. J. Lee, E. J. Min, Y. Kim, H. Y. Kim, and B. H. Lee, "Evaluating and identifying pearls and their nuclei by using optical coherence tomography," Opt. Express **18**(13), 13468–13477 (2010).
26. Y. Zhou, T. Liu, Y. Shi, Z. Chen, J. Mao, and W. Zhou, "Automated Internal Classification of Beadless Chinese ZhuJi Freshwater Pearls based on Optical Coherence Tomography Images," Sci. Rep. **6**(1), 33819 (2016).
27. M. J. Ju, S. J. Lee, Y. Kim, J. G. Shin, H. Y. Kim, Y. Lim, Y. Yasuno, and B. H. Lee, "Multimodal analysis of pearls and pearl treatments by using optical coherence tomography and fluorescence spectroscopy," Opt. Express **19**(7), 6420–6432 (2011).
28. A. Y.-M. Lin, P.-Y. Chen, and M. A. Meyers, "The growth of nacre in the abalone shell," Acta Biomater. **4**(1), 131–138 (2008).
29. W. Drexler, J. G. Fujimoto, and J. G. Fujimoto, *Optical Coherence Tomography: Technology and Applications*, Technology and Applications (Springer, 2008).
30. A. Hojjatoleslami and M. R. N. Avanaki, "OCT skin image enhancement through attenuation compensation," Appl. Opt. **51**(21), 4927–4935 (2012).
31. G. J. Tearney, M. E. Brezinski, J. F. Southern, B. E. Bouma, M. R. Hee, and J. G. Fujimoto, "Determination of the refractive index of highly scattering human tissue by optical coherence tomography," Opt. Lett. **20**(21), 2258–2260 (1995).
32. J. Kang, P. Feng, X. Wei, E. Y. Lam, K. K. Tsia, and K. K. Y. Wong, "102-nm, 44.5-MHz inertial-free swept source by mode-locked fiber laser and time stretch technique for optical coherence tomography," Opt. Express **26**(4), 4370–4381 (2018).
33. R. Huber, M. Wojtkowski, and J. G. Fujimoto, "Fourier Domain Mode Locking (FDML): A new laser operating regime and applications for optical coherence tomography," Opt. Express **14**(8), 3225–3237 (2006).
34. J. Schmitt, S. Xiang, and K. Yung, "Speckle in optical coherence tomography," J. Biomed. Opt. **4**(1), 95 (1999).
35. N. Venkatanath, D. Praneeth, B. Maruthi Chandrasekhar, S. S. Channappayya, and S. S. Medasani, "Blind image quality evaluation using perception based features," in *2015 Twenty First National Conference on Communications (NCC)*, (2015), 1–6.
36. D. Micieli, D. Di Martino, M. Musa, L. Gori, A. Kaestner, A. Bravin, A. Mittone, R. Navone, and G. Gorini, "Characterizing pearls structures using X-ray phase-contrast and neutron imaging: a pilot study," Sci. Rep. **8**(1), 12118 (2018).
37. D. Junqing and L. Qinghui, "Research on nondestructive measurement of sea pearls using optical coherence tomography technique," Infrared Laser Eng. **47**(4), 417004 (2018).